Progress in Propulsion Physics **2** (2011) 251-264

COMBUSTION EFFICIENCY OF A POROUS INJECTOR DURING THROTTLING OF A LOx/H_2 COMBUSTION CHAMBER

J. Deeken, D. Suslov, O. Haidn, and S. Schlechtriem

German Aerospace Center (DLR)
Institute of Space Propulsion Langer Grund
Hardthausen 74239, Germany

The effect of throttling on combustion efficiency and stability of a porous injector head has been investigated for the LOx/H_2 propellant combination. Several pressure ramps (PR) ranging from 30 to 100 bar have been used so that a broad range of possible chamber pressures was covered. Regarding the design pressure of 80 bar, this was equivalent to a throttling range of 37.5% to 125%. The hydrogen injection temperature was varied between 50 and 105 K. The oxygen injection temperature was about 115 ± 5 K. All tests were performed at the P8 test bench using a 50-millimeter diameter modular combustion chamber. The combustion efficiency at a hydrogen injection temperature of 105 K varied between 97.5% and 99% and was nearly independent of pressure. For hydrogen at 50 K, the combustion efficiency increased with chamber pressure and ranged from 94% to 97%. The combustion roughness at 50 K was higher than for the 105-kelvin test cases.

1 INTRODUCTION

1.1 Requirements

A key requirement for a useful injector head is its operational flexibility, i. e., the ability to operate over a broad range of thrust levels without major degradation of combustion efficiency and combustion stability. Certain proposed missions, e.g., lander missions, require an engine which delivers a given thrust at a certain time of the flight profile. The engine for the Apollo lunar lander can be throttled to 10% of its nominal thrust [1]. At the same time, degradation of the performance due to throttling has to be avoided. Conventional coaxial injector elements rely on the momentum exchange between fuel and oxidizer due

Article available at http://www.eucass-proceedings.eu or http://dx.doi.org/10.1051/eucass/201102251

to shear forces for the primary atomization. Injector element dimensions are optimized for a certain small operating range. Typical injection velocities are $v_{H_2} = 200$–300 m/s and $v_{O_2} = 20$–30 m/s. For a constant injector geometry, the relevant hydrodynamic parameters of injection, like the velocity ratio of fuel and oxidizer $V_R = v_f/v_o$ or the momentum flux ratio $J = (\rho_f v_f^2)/(\rho_o v_o^2)$, vary with changing the combustion-chamber pressure. The chamber pressure is roughly proportional to the delivered thrust. A deep throttling of an engine equipped with coaxial injector elements could cause off-nominal operation leading to performance degradation [2]. An injector design which is insensitive to the varying injection conditions is preferable for applications which require throttling capability.

1.2 API Approach

At the DLR Institute of Space Propulsion Lampoldshausen, an injector head design is investigated which relies on an increased initial contact surface between fuel and oxidizer to promote atomization, while classical injector heads with coaxial elements rely on shear forces close to the injector head. The increase in the contact surface between fuel and oxidizer is achieved by injecting the oxidizer (Liquid Oxygen, LOx) through many small tubes in a parallel showerhead configuration. This injector head design has been investigated with an optically accessible combustion chamber [3]. The individual LOx jet diameter for the injector head which is presented here was 1.5 mm. The fuel — in this case, hydrogen — was injected through a porous faceplate. Further on, this assembly will be called API. Due to the large injection area, hydrogen injection velocities were very low. Typically, they were in the range of 4 to 12 m/s, depending on the injection temperature. Liquid oxygen injection velocities typically ranged between 5 and 17 m/s for chamber pressures of 30 and 100 bar, respectively. Since no significant propellant acceleration by the injector head was needed for the atomization, the pressure drops for the fuel and the oxidizer across the injector could be kept comparably low. For hydrogen temperature of 105 K, the hydrogen pressure drop across the faceplate was below 10% of the chamber pressure. For lower hydrogen injection temperatures, the hydrogen pressure drop decreased further. The opportunity to design for low hydrogen pressure drops has several advantages regarding the design of an engine. With the API concept, the engine cycle can be optimized by either an increased chamber pressure or a more efficient turbopump.

Due to the small difference in the velocity between the LOx jet and the surrounding H_2, initial Weber numbers were very low compared to coaxial injectors. For a porous injector using the API design, the atomization was dominated by the disintegration of the LOx jet by the accelerating combustion gases. The velocity difference between the oxygen jets and the combustion gases increased

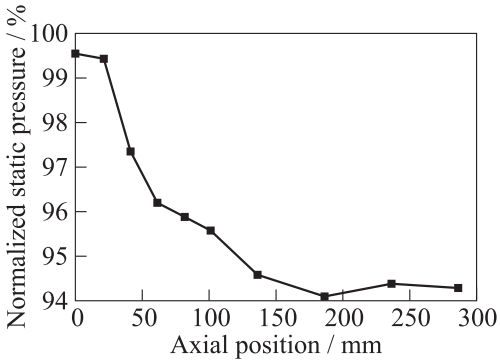

Figure 1 Axial pressure distribution for PR III (see subsection 2.2) at 80-bar theoretical total chamber pressure

rapidly with axial distance from the injector head and promoted mixing by shear forces. The axial mean velocity profile for the combustion gases is an important parameter for the atomization. Figure 1 shows the results of the static pressure measurements along the wall. At a location of 130 mm downstream of the injector faceplate, the chamber pressure converges to a near-constant value. Propellant reaction and acceleration of the combustion gases were essentially complete at this axial position and the chamber velocity approached the value which is theoretically determined by an equilibrium calculation using NASA's CEA code [4]. The combustion gases were accelerated from nearly zero velocity to about 320 m/s within a distance of 130 mm. In principle, the task of mixing of the propellants was transferred from the injector head to the combustion process itself.

2 EXPERIMENTAL SETUP

2.1 Combustion Chamber and Sensor Equipment

The data presented in this paper were determined using the DLR subscale combustion chamber model B and the porous injector head API68 (Advanced Porous Injector). The LOx was injected via 68 small diameter tubes ($d_{\text{outer}}/d_{\text{inner}}$ = 2.0 [mm] / 1.5 [mm]) while the fuel was injected through the whole area of the porous faceplate, which was made of sintered bronze spheres. The permeability of this material resulted in a fuel pressure drop of 5% to 10% of the combustion chamber pressure, depending on the fuel injection temperature. The modular combustion chamber with a diameter of d_{cc} = 50 mm consisted of

one measurement segment (length 100 mm), four standard segments (length 50 mm), and a nozzle segment with a throat diameter of 28 mm. The contraction ratio was $\varepsilon_c = A_{cc}/A_t \approx 3.19$. The total combustion chamber length was 328 mm with a value of $L^* = 1009$ mm. The 100-millimeter measurement segment featured 9 static pressure sensors with an axial spacing of 10 mm, which allowed for a high spatial resolution regarding the static pressure measurements. In addition to these static pressure sensors, one dynamic pressure sensor and one thermocouple close to the chamber wall were employed in the measurement segment. All standard 50-millimeter segments were equipped with one static pressure sensor, one dynamic pressure sensor, and one thermocouple, each positioned at half the segment length. Each segment was water cooled. A calorimetric determination of the heat flux in a segment was possible due to the application of thermocouples and flowmeters in the individual water feed lines. Static as well as dynamic pressure sensors were located about 200 mm away from the combustion chamber and were connected via tubes with an inner diameter of 4 mm. This volume inside the connecting tubes acted as a damper for pressure oscillations. Thus, the amplitude measurements were unreliable and could be only used for qualitative information. Measured frequencies were not affected by the connecting tubes. The data from the static pressure sensors were sampled at a rate of 100 Hz, while the dynamic pressure data were sampled at 100 kHz.

Alternating the position of the measurement segment allowed for high resolution pressure measurements at any axial position in the combustion chamber. The arrangement in which the measurement segment was located directly behind the injector head (position: 0–100 mm) will be designated configuration I, while the configuration in which the measurement segment was located at an axial position of 100–200 mm will be referred to as configuration II.

Due to the encouraging results of an application of an uncooled sensor ring which was located directly downstream of the injector head during a test campaign with the combustion chamber model G, later test runs also used such a sensor ring. This uncooled copper ring (length 11 mm) was equipped with four dynamic pressure sensors at certain angular positions to allow for a phase determination in case transversal modes of combustion instability are detected. The use of this additional sensor ring increased the combustion chamber length to 339 mm and the value of L^* to 1044 mm. The position of the measurement segment was identical to configuration I. This arrangement will be referred to as configuration III. The dynamic pressure sensors applied in the sensor ring were located 10 mm away from the combustion chamber. Former experiments with a 180-millimeter diameter combustion chamber employing a similar sensor arrangement indicated that a closer distance was likely to endanger the sensor. The enclosed volume of combustion gases in the 10-millimeter long cavity was considered small enough to have a negligible effect on pressure am-

Table 1 Configurations of combustion chambers (throat diameter 28 mm, contraction ratio 3.19)

Configuration	Segment used	Chamber length to troat, mm	L^*, mm
I	Measurement segment, 4 standard segments, nozzle	328	1009
II	2 standard segments, measurement segment, 2 standard segments, nozzle	328	1009
III	High-frequency sensor ring, measurement segment, 4 standard segments, nozzle	339	1044

plitude measurements. The described configurations are displayed in Table 1. The test runs presented in this paper were performed with configurations II and III.

2.2 Operating Conditions

To investigate the throttling capability of the described injector head, multiple test runs were performed. Pressure ramps, which vary the chamber pressure at a constant rate by a variation of the propellant mass flow rate allowed investigating combustion efficiency and stability over a wide range of operating con-

Table 2 Operating conditions

	Configuration	p_{cc}, bar	ROF	T_{H_2}, K	T_{O_2},K
PR I	III	30–100	4.96–5.01	47.4–53.3	113.4–119.3
PR II	II	100–30	4.85–5.31	99–110.7	113.3–117.6
PR III	III	100–30	4.75–5.17	99.4–110.5	112.8–117.5
	u_{inj,H_2}, m/s	u_{inj,O_2}, m/s	$\Re_{inj,O_2}$	1L mode, Hz	1T mode Hz
PR I	3.9–9.6	5.4–16.9	75,469–212,130	2405–2438	16,306–16,527
PR II	9.6–11.9	5.3–17.2	69,765–224,681	2484–2534	16,294–16,623
PR III	9.8–11.9	5.3–17.2	69,759–224,200	2395–2454	16,236–16,636

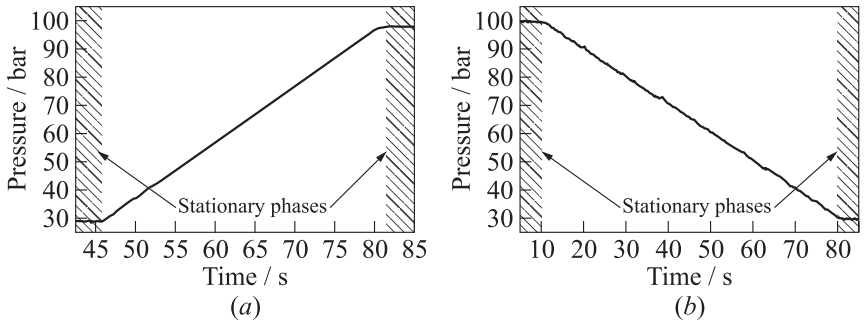

Figure 2 Static pressure at the faceplate: (a) PR I; and (b) PR II and PR III

ditions. The nominal point of operation for the investigated API injector head was 80 bar. A PR ranging from 30 to 100 bar led to a throttling range of 37.5% to 125%. Injection conditions for three PR are presented in Table 2. All values except pressure are the minimum and maximum values encountered during the ramp test. The propellant mixture ratio (ROF) was kept constant at ROF = 5. Pressure ramp I was performed using hydrogen at approximately 50 K ("liquid" hydrogen, LH_2) and the pressure was varied at a rate of 2 bar/s. Pressure ramps II and III used the same sequence and target values for pressures, temperatures, and mass flow rates. Hydrogen was injected at approximately 105 K and the pressure change rate was −1 bar/s. Pressure ramp II used the chamber configuration II (without the sensor ring), while PR III used the chamber configuration III (with the sensor ring). Static pressure readings at the faceplate are presented in Fig. 2. Before and after each pressure ramp, injection conditions were held constant for at least 5 s, which ensured thermal equilibrium in the chamber.

3 EXPERIMENTAL RESULTS

3.1 Combustion Efficiency

3.1.1 Analysis

To measure the quality of the whole combustion process in a rocket combustion chamber, the characteristic velocity c^* was introduced and defined as

$$c^* = \frac{p_{0,\mathrm{cc}} A_t}{\dot{m}} .$$

With the characteristic velocity, an efficiency η_{c^*} was defined as

$$\eta_{c^*} = \frac{c^*_{\text{exp}}}{c^*_{\text{theo}}} .$$

This efficiency represents the ratio of the experimentally achieved value for c^* and the theoretically possible value. The theoretical value for c^*_{theo} or $p_{0,\text{theo}}$ was obtained by assuming a complete combustion of all propellants and chemical equilibrium in the combustion chamber. The ideal combustion chamber values were computed using CEA code. This code assumes zero injection velocity for the calculation of $p_{0,\text{theo}}$. Since the mass flow rate and the nozzle throat area were equal for the theoretical and experimental cases, the calculation of η_{c^*} reduced to

$$\eta_{c^*} = \frac{p_{0,\text{exp}}}{p_{0,\text{theo}}} = \frac{p_{0,\text{EOC,exp}}}{p_{0,\text{EOC,theo}}} . \tag{1}$$

For efficiency determination, a pressure sensor was chosen located directly ahead of the nozzle contraction. This location was named EOC (End Of Combustion). The measured static pressure had to be related to a total pressure at this axial position, while the theoretical total pressure determined for a negligible chamber velocity had to be corrected for total pressure losses due to the nonisentropic nature of combustion. This correction is justified since the losses in total pressure due to nonisentropic combustion cannot be attributed to the injector head but to the combustion chamber contraction ratio [5]. The Mach number at the EOC location was determined using the contraction ratio and the ratio of the specific heats γ_{EOC}. The acceleration in the nozzle contraction was assumed to be isentropic:

$$\varepsilon_{\text{c}} = \frac{A_{\text{cc}}}{A_t} = \frac{1}{\text{M}_{\text{EOC}}} \left[\frac{2}{\gamma_{\text{EOC}} + 1} \left(1 + \frac{\gamma_{\text{EOC}} - 1}{2} \, \text{M}^2_{\text{EOC}} \right) \right]^{(\gamma_{\text{EOC}}+1)/(2(\gamma_{\text{EOC}}-1))} .$$

The ratio of the total and the static pressure at the EOC location was

$$\frac{p_{0,\text{EOC,exp}}}{p_{\text{EOC,exp}}} = \left(1 + \frac{\gamma_{\text{EOC}} - 1}{2} \text{M}^2_{\text{EOC}} \right)^{\gamma_{\text{EOC}}/(\gamma_{\text{EOC}}-1)} . \tag{2}$$

The total pressure loss due to the acceleration of the combustion gases from zero velocity to M_{EOC} was calculated according to [5]:

$$\frac{p_{0,\text{theo}}}{p_{0,\text{EOC,theo}}} = \frac{1 + \gamma_{\text{EOC}} \text{M}^2_{\text{EOC}}}{(1 + (\gamma_{\text{EOC}} - 1)/2)^{\gamma_{\text{EOC}}/(\gamma_{\text{EOC}}-1)}} . \tag{3}$$

Combining equations (1), (2), and (3) resulted in

$$\eta_{c^*} = \frac{p_{\text{EOC,exp}}}{p_{0,\text{theo}}} \left(1 + \gamma_{\text{EOC}} \text{M}^2_{\text{EOC}} \right) . \tag{4}$$

The combustion efficiency was calculated using Eq. (4), the static pressure at the EOC location, and the propellant mass flow rates and temperatures measured during the hot run for the determination of $p_{0,\mathrm{theo}}$. For a detailed analysis several loss factors had to be taken into account.

- pressure losses due to wall friction were not considered in this analysis;
- a considerable amount of heat was lost due to the cooling of the combustion chamber segments. This amount was in the range of 5% of total released heat. The quantification of the effect of the heat loss on the total pressure profile in the combustion chamber required a detailed analysis. The equilibrium composition of the combustion gases, changed in axial direction, while the heat capacity of the mixture varied accordingly. At the same time the heat transfer to the wall was a function of the axial distance. Such a detailed analysis was beyond the skope of this work. The assumption of adiabatic walls led to a maximum total temperature and pressure for the estimation of the ideal total chamber pressure and, therefore, to the most conservative estimate for the combustion efficiency. To keep the heat flux variations during a test at a minimum, the cooling water mass flow rate was nearly proportional to the propellant mass flow rate and, thus, the chamber pressure. This allowed for a comparison of different operating conditions during one test run in respect to the heat losses due to cooling;
- at the P8 test facility, oxygen was pressurized using nitrogen, which resulted in a change in the equilibrium composition. The measured mass flow rate for oxygen included a certain percentage of nitrogen, which did not contribute to the energy release during combustion. Assuming an oxygen mass fraction of unity led to the maximum theoretical total chamber pressure and to the minimum combustion efficiency since $\eta_{c^*} = p_{0,\mathrm{exp}}/p_{0,\mathrm{theo}}$. A simple correction factor for the combustion efficiency was calculated as a function of oxygen mass fraction and theoretical total chamber pressure using NASA's CEA code. Results are shown in Fig. 3 for a hydrogen temperature of 50 K. For the test runs presented here, measurements indicate an oxygen mass fraction between 95% and 97%. This correction factor was not included in the presented values for the combustion efficiency; and
- the exact value of the nozzle throat diameter during hot run was an uncertainty in the calculation of the theoretical total chamber pressure which determined the combustion efficiency. During the hot run, the heat load to the nozzle wall caused a thermal strain and the nozzle geometry was changing. This thermal strain, the pressure loads, and the restraint due to the outer supporting structure of the combustion chamber determined the change in the nozzle throat diameter. A quantitative analysis of the resulting change in the nozzle throat diameter required the use of Finite

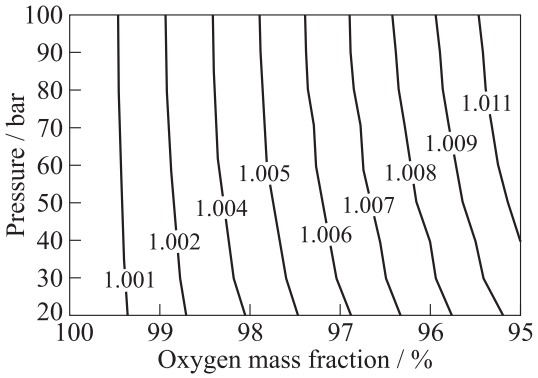

Figure 3 Correction factor for nitrogen mass fraction

Elements Methods (FEM). This task was not performed for the calculation of the data presented here. The nozzle throat diameter used for the calculation of the combustion efficiency was 28 mm. A detailed analysis of the influence of the heat load on the nozzle geometry is planned for the near future.

Only the relative changes in combustion efficiency are important to quantify the throttling capabilities of an injection system. The loss factor due to the nitrogen pressurization could introduce a maximum deviation of approximately 0.15% during ramping between 30 and 100 bar. The other loss factors mentioned were assumed to be constant.

3.1.2 Results

The combustion efficiency was calculated for the PR described in subsection 2.2. The results are presented in Fig. 4. The bigger symbols represent the values of the stationary operating conditions just before and after the PR. For PR I ($T_{H_2} \approx 50$ K), η_{c^*} ranges from 94% to 97% with increasing the theoretical total chamber pressure. The PR II and PR III with $T_{H_2} \approx 105$ K show the opposite trend but less pronounced. The values of η_{c^*} range from 99% to 97.5%. The comparison of the combustion efficiencies of the stationary operating conditions shows that for PR II and PR III, the combustion efficiencies are essentially the same for 30 and 100 bar, respectively. For the PR I, the difference in combustion efficiency between the lower and upper operating points is also lower than the span of the values for the PR itself. This effect can be attributed to the dynamic behavior of the P8 test bench. The mass-flow measurement, which is used to calculate the theoretical total chamber pressure, was made at least 6.5 m away

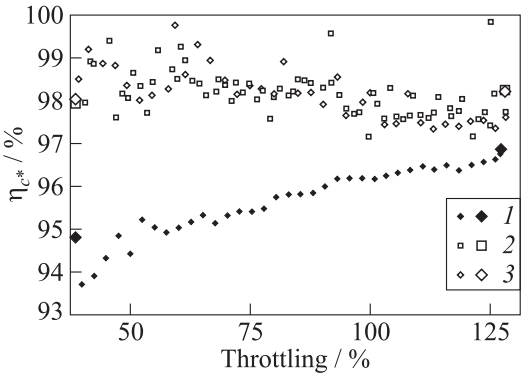

Figure 4 Calculated combustion efficiencies (uncorrected): *1* — PR I; *2* — PR II; and *3* — PR III; large symbols refer to stationary operating conditions

from the injector head. For a PR with positive pressure increment like the PR I, the actual mass flow rate at a certain time at the injector head was less than the measured one. This led to a negative bias for the calculation of the combustion efficiency. In case of PR II and PR III with decreasing chamber pressure, the same effect led to a positive bias. The comparison between PR I and the corresponding steady-state operating points shows that this bias was stronger at low chamber pressures. For constant-rate PR, the pressure ratio between two points in time and, therefore, the deviation of the actual mass flow rate from the measured mass flow rate was larger at lower absolute pressures. Pressure ramps II and III were performed with a pressure change rate of −1 bar/s, while PR I had a rate of 2 bar/s, leading to a more pronounced dynamic bias for PR I.

For a quantitative determination of this bias, a detailed analysis of the filling processes encountered during the transient phases has to be performed. A transfer function including the various different hydraulic elements between the position of the mass flow measurement and the injector head faceplate is needed. This is beyond the scope of this publication. Yet, it can be assumed that the correction of this dynamic bias would lead to lower η_{c^*} values for PR II and PR III and higher η_{c^*} values for PR I. Since the effect of the dynamic bias is stronger at lower chamber pressures, a correction of the dynamic bias results in a weaker pressure dependency of η_{c^*}.

3.2 Combustion Stability

The use of dynamic pressure sensors allows for the determination of combustion stability over the range of operating conditions. Combustion stability is

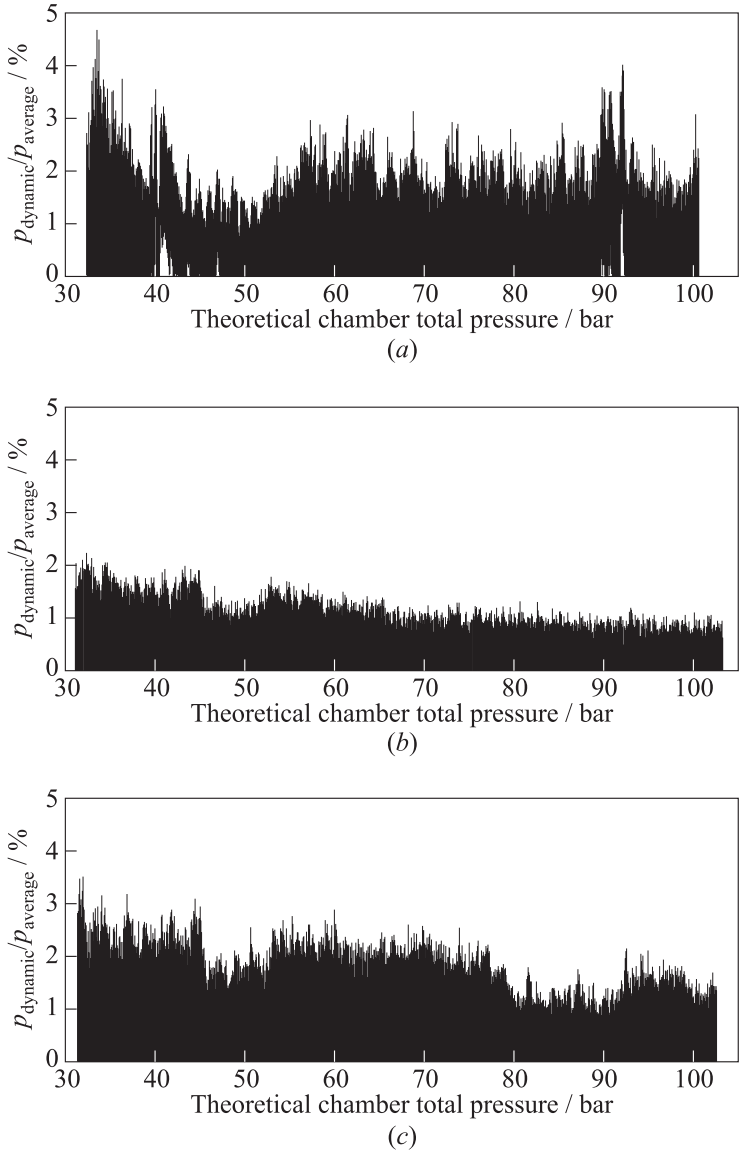

Figure 5 Combustion roughness for PR I to III ((*a*) to (*c*)): (*a*) $T_{H_2} = 50$ K, chamber configuration III (with sensor ring); (*b*) $T_{H_2} = 105$ K, chamber configuration II (without sensor ring); and (*c*) $T_{H_2} = 105$ K, chamber configuration III (with sensor ring)

most commonly determined using dynamic pressure readings. Pressure oscillations exceeding 5% of static chamber pressure indicate a rough combustion or instability [6]. Figure 5 shows the absolute values for the dynamic pressure normalized by a sliding average of the static pressure measured directly behind the injector face. For all PR investigated, the combustion roughness was below 5% for the whole range of the individual PR. The difference in amplitude between PR II and PR III can be attributed to the dampening effect of the gas volume enclosed in the tubes used for the dynamic pressure sensors in configuration II (see subsection 2.1). During PR II and PR III, combustion roughness increased towards lower chamber pressures. Such a clear trend was not observed for PR I, although the highest combustion roughness occurred at low chamber pressures around 30 bar. All pressure ramps show a slight decrease in combustion roughness around 50-bar theoretical total chamber pressure, which is in the proximity of the critical pressure for oxygen.

A preliminary spectrum analysis showed no distinct excitation of characteristic chamber frequencies or their overtones (see Table 2). Instead, dominant frequencies were observed in the range of 40–100 Hz. The P8 test facility is known to introduce frequencies in this range via the propellant feed lines.

3.3 Wall Heat Flux

Wall heat fluxes were determined using the cooling-water mass flow rate for each individual segment and the corresponding temperature change. For a segment in thermal equilibrium, this measured value was equal to the heat flux at the combustion chamber wall. For the steady-state points of PR I and PR III, wall heat fluxes normalized by their individual maximum value are given in Fig. 6. The data points at $x = 339$ mm represent the nozzle throat position. For

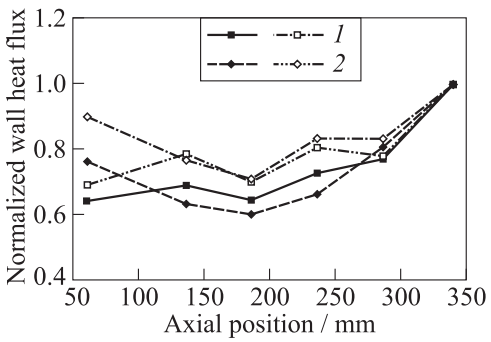

Figure 6 Wall heat fluxes determined for the steady-state points of PR I (black signs) and PR III (empty signs): *1* — 100 bar; and *2* — 30 bar

identical pressure levels, the normalized heat fluxes for PR I in the cylindrical chamber section are lower than those for PR III. This can be explained by the lower combustion efficiency measured for the 50-kelvin ramp. For PR I, more unburned oxidizer was present in the nozzle section than for PR III. This oxidizer was able to react in the nozzle section, which increased the heat loads to the nozzle wall, therefore increasing the ratio between the nozzle section and the cylindrical part.

4 CONCLUDING REMARKS

The operation of the porous injector of API design has been demonstrated using LOx/H_2 propellants. The chamber pressure was varied over a broad throttling range of 37.5% to 125% of nominal chamber pressure (80 bar). The test runs were performed using a 50-millimeter diameter modular combustion chamber. The lowest hydrogen injection temperature was 50 K. The combustion efficiency has been calculated for transient and stationary phases. Uncorrected values of the combustion efficiency at a hydrogen injection temperature of 105 K and 50 K ranged from 99.5% to 98.5% and from 94% to 97%, respectively. The pressure dependency of these values is expected to decrease after suitable correction for the dynamic behavior of the P8 test bench. Combustion roughness was measured directly behind the faceplate and was below 5% of the mean chamber pressure at all conditions. The wall heat fluxes were determined using a calorimetric method. Heat fluxes close to the injector head were comparable to those further downstream. This indicates an onset of the combustion region close to the injector head.

The data presented herein indicate that a porous injector head of API design is well suited for applications requiring deep throttling that demand a drastic change of injection conditions. In terms of the combustion efficiency and stability, the new injector-head design presented here shows low sensitivity to variations in injection conditions.

ACKNOWLEDGMENTS

The authors would like to thank the P8 team for their contribution to the success of the presented test campaign.

REFERENCES

1. Dressler, G. A., and J. M. Bauer. 2000. TRW pintle engine heritage and performance characteristics. *36th AIAA/ASME/SAE/ASEE Joint Propulsion Conference and Exhibit*. Huntsville.

2. Bazarov, V. G. 1994. Throttleable liquid propellant engines swirl injectors for deep smooth thrust variation. *30th AIAA/ASME/SAE/ASEE Joint Propulsion Conference and Exhibit*. Indianapolis.
3. Lux, J., D. Suslov, and O. Haidn. 2008. On porous liquid propellant rocket engine injectors. *Aerospace Sci. Technol.* 12:469–77.
4. Gordon, S., and B. McBride. 1994. Computer programm for calculation of complex chemical equilibrium compositions and applications. NASA RP-1311.
5. Sutton, G. P., and O. Biblarz. 1963. *Rocket propulsion elements*. 3rd ed. John Wiley & Sons.
6. Harrje, T. P. 1972. *Liquid propellant rocket combustion instability*. Washington, D.C. NASA SP-194.